Interface engineering of (Ni, Fe)S$_2$@MoS$_2$ heterostructures for synergetic electrochemical water splitting

Yunke Liu[a,1], Shan Jiang[a,1], Shijin Li[a], Lei Zhou[a], Zhenhua Li[a], Jianming Li[b], Mingfei Shao[a,*]

[a] State Key Laboratory of Chemical Resource Engineering, Beijing University of Chemical Technology, Beijing, 100029, China
[b] Petroleum Geology Research and Laboratory Center, Research Institute of Petroleum Exploration & Development (RIPED), PetroChina, Beijing, 100083, China

ARTICLE INFO

ABSTRACT

Water splitting to generate hydrogen is a promising and sustainable process, whereas is limited by the large overpotential of electrode materials for cathode hydrogen evolution reaction (HER) and anode oxygen evolution reaction (OER). Here we present an interface engineering strategy to construct efficient bifunctional electro-catalyst based on (Ni, Fe)S$_2$@MoS$_2$ heterostructrues for water-splitting process. The as-prepared (Ni, Fe)S$_2$@MoS$_2$ catalyst gives remarkable electrochemical activity and durability under alkaline environments, with a low overpotential of 130 mV for HER and 270 mV for OER to deliver the current density of 10 mA cm^{-2}, respectively. In combination with *in-situ* Raman spectra, we demonstrate that the constructed interfacial active sites are favorable to the formation of S-H$_{ads}$, which synergistically lower the chemisorption energy of the intermediates of HER and OER, thereby facilitating the electrocatalytic overall water splitting. Furthermore, we regulate the interface of (Ni, Fe)S$_2$@MoS$_2$ and electrolyte through changing the composition of electrolyte to achieve much longer electrochemical stability of this hybrid sulfide electrocatalyst.

1. Introduction

Hydrogen is widely regarded as one of the most appealing energy resources since its renewable and environmental-friendly properties [1–3]. Among kinds of approaches to generate hydrogen, electro-chemical water splitting is a promising pathway benefiting from a large number of water resources and high-purity hydrogen production [4–6]. Currently, precious metal electrode materials such as Pt and RuO$_2$/IrO$_2$ have been demonstrated with perfect electrocatalytic performance for hydrogen evolution reaction (HER) and oxygen evolution reaction (OER), respectively [7–9]. However, the shortage, exorbitant price and poor durability of noble metals hinder their further practical applica-tions. Consequently, much attention have been focused on earth-ample alternatives with satisfactory catalytic performance and durability [10–12]. Nevertheless, very few of catalysts are effectively capable of catalyzing both OER and HER because OER catalysts exhibit high ac-tivities in alkaline electrolytes while most HER catalysts prefer acidic environments. Thus, the development of efficient bifunctional electrode materials for overall water splitting in the same electrolyte assigns more significance, but still remains a challenge.

Among various materials, transition metal dichalcogenides (TMDs) have shown excellent HER performance [13–16]. For instance,

molybdenum disulfide (MoS$_2$) with trigonal prismatic (2H) and octa-hedral phases (1T) have been regarded as promising highly active HER catalysts in acidic media [17,18]. Regrettably, their OER activities are subject to high overpotential and sluggish reaction kinetics, which exert negative influence upon overall water splitting [19,20]. Furthermore, one major issue for MoS$_2$ besides electrocatalytic activity is their re-duced stability because a high sulfur leaching rate makes 2H-MoS$_2$ unstable and the intrinsic metastable properties of 1T-MoS$_2$ [21,22]. On the contrary, NiFe mixed compounds show remarkable OER activities in basic conditions but display poor HER performances [23–25]. This in-spired us to explore highly active and improved stability electrocatalyst for both HER and OER based on MoS$_2$ and NiFe compounds. To improve the activity for water-splitting process, it is imperative to reduce energy of the formation of H* and OH$^-$ intermediates. This implies the im-portance of interface engineering of heterostructures containing HER and OER catalysts, which will effectively modify the electronic en-vironment for synchronous chemisorption of both H* and OH$^-$ inter-mediates on the surface. In addition, regulating the interface of elec-trode/electrolyte to prohibit the interfacial sulfide oxidation as well as leaching of S is also promising for durable sulfide-based electro-catalysts, which is rarely considered.

Herein, we design and synthesize the heterostructures consisting of

---

* Corresponding author.
E-mail address: shaomf@mail.buct.edu.cn (M. Shao).
[1] These authors contribute equally to this work.

(Ni, Fe)S$_2$ nanoboxes and MoS$_2$ nanoarrays *via* a hydrothermal synthesis based on NiFe-LDH precursor, which display largely improved activity and durability towards water-splitting process. Typically, the (Ni, Fe)S$_2$@MoS$_2$ heterostructures exhibit low overpotentials of 130 mV and 270 mV to reach the current density of 10 mA cm^{-2} for HER and OER respectively, which is comparable to the best bifunctional electrocatalysts reported previously. *In-situ* Raman spectra are applied to record the process of forming S-H$_{ads}$, which reveals that the interface of heterostructures is advantageous to form stable H* intermediates and simultaneously to stable OH$^-$ intermediates to promote the overall water splitting. Additionally, the stability of (Ni, Fe)S$_2$@MoS$_2$ heterostructures is further significantly improved by introducing of ionic S in the electrolyte, which effectively relieves the leaching of atomic S in the sulfides.
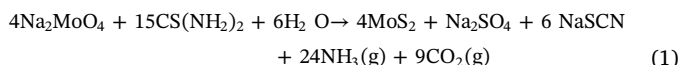
2. Experimental section

2.1. Synthesis of (Ni, Fe)S$_2$@MoS$_2$ heterostructures

2.1.1. Preparation of NiFe-LDH arrays

The NiFe-LDH arrays on carbon fiber paper (CFP) were obtained by a hydrothermal method [26]. In the method, Ni(NO$_3$)$_2$.6H$_2$O (1.28 mM), Fe(NO$_3$)$_3$.H$_2$O (0.33 mM), urea (2.86 mM), sodium citrate (0.14 mM) were stirred and mixed completely to obtain clear aqueous of 60 mL. Carbon fiber paper (CFP) was preprocessed with HNO$_3$ to guarantee a hydrophilic surface. Then CFP was immersed into aforementioned aqueous in a 80 mL stainless-steel autoclave, reacting at 120 °C for 18 h, later cooling down to 25 °C naturally. An orange yellow film formed on CFP substrate, which was cleaned with deionized water and ethanol for three times, later dried at 50 °C overnight.

2.1.2. Synthesis of (Ni, Fe)S$_2$@MoS$_2$ heterostructures

The (Ni, Fe)S$_2$@MoS$_2$ heterostructures were synthesized by sulfured process of (Ni, Fe)-LDH precursor. In a normal process, thioacetamide (PAA) (6.25 mM), Na$_2$MoO$_4$·2H$_2$O (1.25 mM) mixed fully to form a transparent aqueous of 50 mL and transfer to Teflon-lined stainless-steel autoclave, synthesized as (Ni, Fe)S$_2$@MoS$_2$ (Mo:S-1:5). Then the as-prepared NiFe-LDH/CFP film was immersed into aforementioned aqueous, heating at 200 °C for 8 h, afterwards cooling down to 25 °C. A black film with metallic luster was prepared on CFP and was cleaned with distilled water and ethanol for three times, later dried at 50 °C overnight. The chemical equation of formation of MoS$_2$ is as following:

$$4Na_2MoO_4 + 15CS(NH_2)_2 + 6H_2O \rightarrow 4MoS_2 + Na_2SO_4 + 6\,NaSCN$$
$$+ 24NH_3(g) + 9CO_2(g) \tag{1}$$

2.2. Characterization

X-ray diffraction (XRD) patterns were characterized on a Shimadzu XRD-6000 diffractometer *via* Cu Kα source (λ = 0.15419 nm). The morphology was recorded *via* SEM (Zeiss SUPRA 55) with elementary disperse spectroscope (EDS) mapping analysis. Transmission electron microscope (TEM) and high-resolution transmission electron microscopes (HRTEM) was investigated by a Philips Teecanai 20 and JEOL JEM-2010, which an accelerating voltage is 200 kV. Raman spectra were recorded on a confocal Raman microspectrometer (Renishaw, inVia-Reflex) equipped with Ar laser (wavelength = 530.5 nm).

2.3. Electrochemical measurements

The electrochemical performances were performed on a CHI 660E electrochemical workstation (Shanghai Chenhua Instrument Co., China) using a conventional three-electrode configuration in 1 M KOH media. (Ni, Fe)S$_2$@MoS$_2$ heterostructrues prepared on carbon fiber paper (CFP) were utilized as the working electrode. Pt wire were used as the counter electrode and Ag/AgCl was employed as reference electrodes. The measured potentials in 1 M KOH (pH = 14) *vs.* Ag/AgCl reference electrode were transformed to the reversible hydrogen electrode (RHE) *via* the Nernst equation:

$$E_{RHE} = E_{Ag/AgCl}^{\theta} + 0.059\,pH + E_{Ag/AgCl} \tag{2}$$

where E_{RHE} represents the potential *vs.* RHE; $E_{Ag/AgCl}^{\theta}$ shows the theoretical potential (0.197 V), and $E_{Ag/AgCl}$ is the experimental potential contrasted to reference electrode; therefore:

$$E_{RHE} = E_{Ag/AgCl} + 1.023\,V \tag{3}$$

For the evaluation of OER and HER performances, linear sweep voltammetry (LSV) was recorded at a scan rate of 1 mV s^{-1} in 1 M KOH. As for electrochemical impedance spectroscopy (EIS), the Nyquist plots of electrochemical impedance spectroscopy (EIS) were studied in the same condition from 10^{-1} to 10^5 Hz at the open circle voltage. The ECSA values were measured through cyclic voltammetry (CV) in the selected non-faradaic range. The current densities have linear relationship against different scan rates (20–120 mV s^{-1}) and the values of the slop were considered as twice of C_{dl}.

3. Results and discussion

3.1. Structural and morphological of (Ni, Fe)S$_2$@MoS$_2$ heterostructures

As shown in Fig. 1a, the synthetic process of (Ni, Fe)S$_2$@MoS$_2$ involves two steps: the hydrothermal synthesis of NiFe-LDH precursor and followed by the synthesis of (Ni, Fe)S$_2$@MoS$_2$ heterostructures. Primarily, well-defined NiFe-LDH nanosheet arrays (NSAs) on carbon
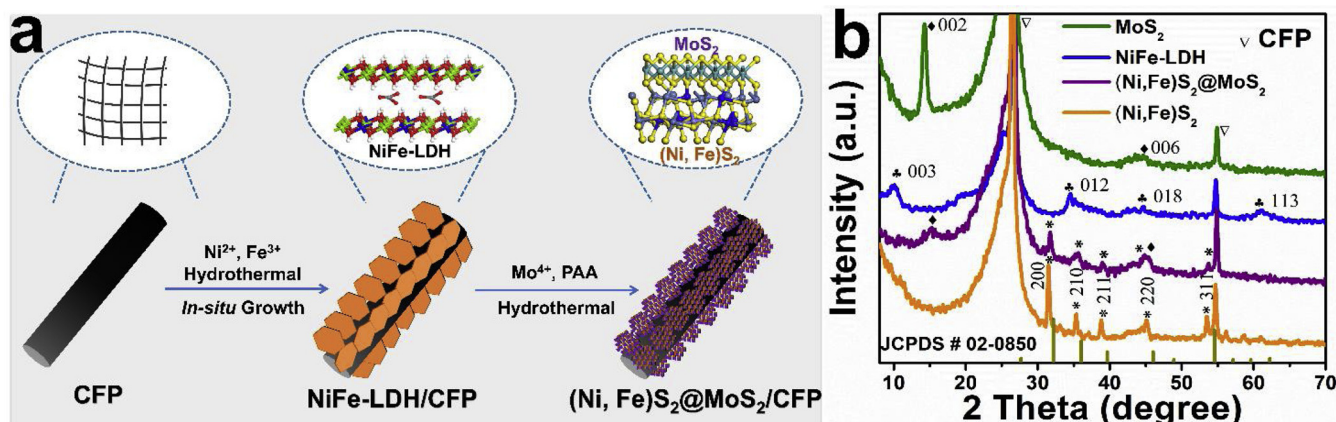

Fig. 1. (a) Illustration for the fabrication of (Ni, Fe)S$_2$@MoS$_2$ heterostructures. (b) XRD patterns of MoS$_2$, (Ni, Fe)S$_2$, (Ni, Fe)S$_2$@MoS$_2$ and NiFe-LDH.

fiber paper (CFP) were obtained by a typical hydrothermal method. Afterwards, the NiFe-LDH NSAs were converted to (Ni, Fe)S_2 nanoboxes and covered with a layer of MoS_2 nanosheets *via* vulcanization process in the solution of thioacetamide (PAA) and sodium molybdate ($Na_2MoO_4 \cdot 2H_2O$). It is noted that the color of the electrode is replaced from light grey to metallic yellow, which indicates the formation of molybdenum compounds (Fig. S1). Four samples of (Ni, Fe)S_2@MoS_2 heterostructures with different interfacial contact areas were obtained *via* a fine control over the Mo content (Mo:S = 0.25, 0.5, 1 and 3, defined as Mo:S-0.25:5, 0.5:5, 1:5 and 3:5, respectively).

The structural information of NiFe-LDH, (Ni, Fe)S_2@MoS_2, (Ni, Fe)S_2 and MoS_2 were illustrated by X-ray diffraction (XRD) in Fig. 1b. The XRD pattern of NiFe-LDH/CFP exhibits a string of (003), (012), (018) reflections, which could be indexed to LDH phase [27]. After the process of vulcanization, the (Ni, Fe)S_2@MoS_2 heterostructures were prepared which show a superimposition of (Ni, Fe)S_2 phase and MoS_2 phase, implying the successful fabrication of (Ni, Fe)S_2 and MoS_2. Typically, the (200), (210), (211), (220) and (311) reflection of (Ni, Fe)S_2 (Ni rich) phase (JCPDS # 02-0850) as well as (002) and (006) reflection of 2H-MoS_2 phase (JCPDS# 37-1492) are clearly observed. It is worth mentioning that the (Ni, Fe)S_2 (Ni rich) phase could be understood as a small amount of Fe doping into the lattice of NiS_2 [28]. The other three samples (Mo:S-0.25:5, 0.5:5 and 3:5) were obtained by adjusting the content of Mo and their XRD patterns (Fig. S2) illustrate the weakened reflections of (Ni, Fe)S_2 and strengthened phase of MoS_2 along with the increase of Mo content.

The scanning electron microscopy (SEM) images of NiFe-LDH NSAs exhibit a ultrathin and uniform network perpendicularly grown on the carbon fiber paper (CFP) with a lateral size of 200 nm (Fig. 2a and e). After the synthesis of (Ni, Fe)S_2@MoS_2 with a lower Mo content, a new thick sheet-like arrays present on the surface of CFP with an intercrossing decorated MoS_2 nanosheets vertically grafting onto the (Ni, Fe)S_2 nanoboxes (Fig. 2b, c and f, g). It is observed that Mo content displays an imperative influence upon the interfacial contact areas and morphologies. As Mo content increased, more MoS_2 nanosheets were formed on the surface of (Ni, Fe)S_2 nanoboxes, which is suggested as the morphologies changed from initial (Ni, Fe)S_2 nanoboxes (Fig. S3a, c) to (Ni, Fe)S_2 nanoboxes decorated with different amount of MoS_2 nanosheets (Fig. 2b–d, f–h), eventually to MoS_2 nanosheets fully covering (Ni, Fe)S_2 nanoboxes (Fig. S3b, d). Element mapping analysis of (Ni, Fe)S_2@MoS_2 reveals a uniform dispersion of Mo, S, Ni, and Fe on carbon fiber paper, indicating the homogeneous distribution of MoS_2 nanoarrays on (Ni, Fe)S_2 nanoboxes (Fig. 2i). The transmission electron microscopic (TEM) image of (Ni, Fe)S_2@MoS_2 (Fig. 2j) further confirms that the hydrothermal synthesis of MoS_2 nanosheets are decorated uprightly on the plane of (Ni, Fe)S_2 nanoboxes (Fig. S5a, b). It is worth mentioning that there are some discontinuous stripes in the crystal fringes, which demonstrates the fact that Fe is doping into the lattice of NiS_2. Additionally, high resolution TEM (HRTEM) shows lattice fringes with 0.27 nm in the inner layer of nanoboxes and 0.62 nm in the decorated layer, corresponding to the (Ni, Fe)S_2 (200) and MoS_2 (002) planes, respectively (Fig. 2k). To further understand the mechanism of the formation of such heterostructures, we prepared (Ni, Fe)S_2@MoS_2 with different synthetic time. As shown in Fig. S4, when the synthetic time is short at 0.5 h, it could not observe obvious morphological nanoarrays. Subsequently, when the synthetic time increased to 2 h, it is clear that the nanoarrays of (Ni, Fe)S_2 nanoboxes decorated with MoS_2 nanosheets have been formed. With increasing the reaction time to 4 h, more MoS_2 have been synthesized and covered on the surface of (Ni, Fe)S_2 nanoboxes.

To investigate the influence of interfacial electronic interaction between inner (Ni, Fe)S_2 and decorated MoS_2, X-ray photoelectron spectroscopy (XPS) was employed for (Ni, Fe)S_2, MoS_2 and (Ni, Fe)S_2@MoS_2 heterostructures. The pristine (Ni, Fe)S_2 sample shows the presence of Ni, Fe, S and O elements and MoS_2 sample demonstrates Mo, S and O elements; while the (Ni, Fe)S_2@MoS_2 core-shell sample confirms the co-existence of Ni, Fe, S, Mo and O elements, implying the successful fabrication of (Ni, Fe)S_2 and MoS_2 (Fig. S6). Fig. 3a displays the
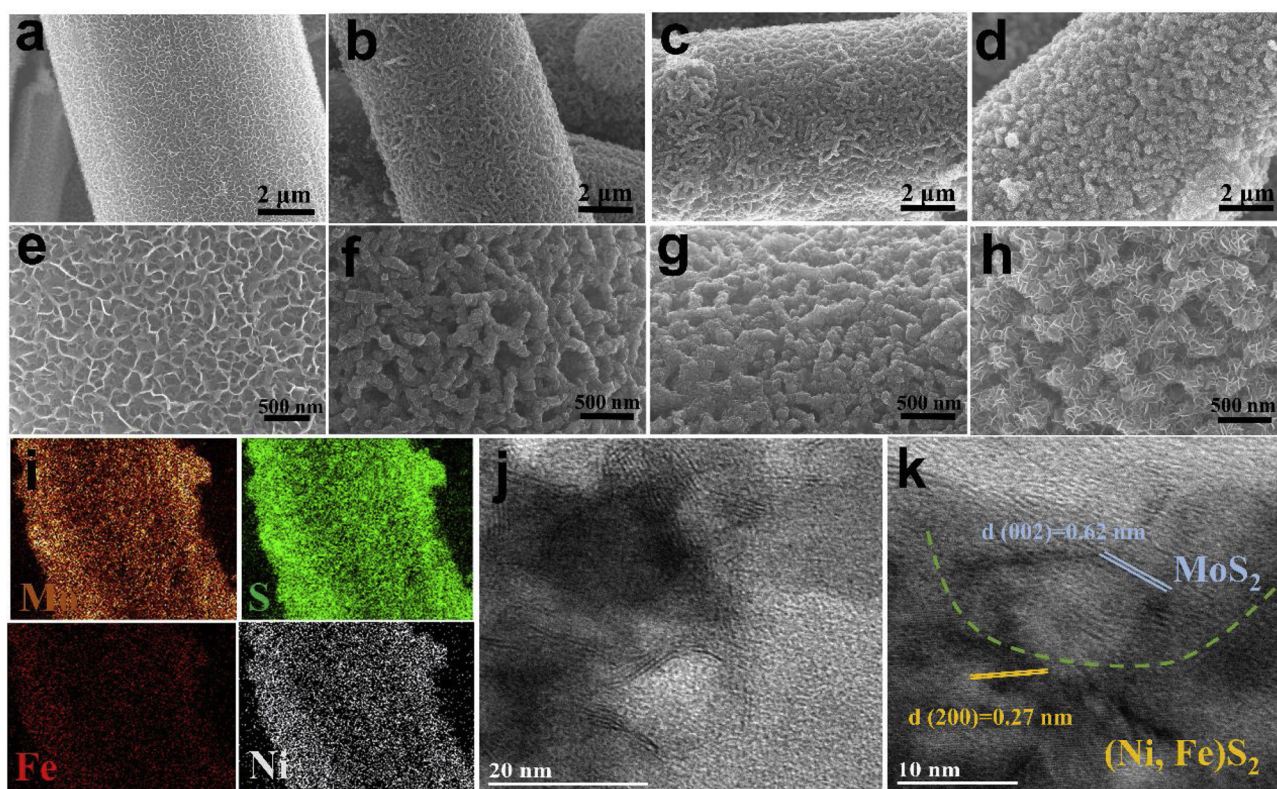

Fig. 2. SEM images of (a) NiFe-LDH, (b) (Ni, Fe)S_2@MoS_2 Mo:S-0.25:5, (c) (Ni, Fe)S_2@MoS_2 Mo:S-0.5:5, (d) (Ni, Fe)S_2@MoS_2 Mo:S-1:5. (e–h) corresponding magnified SEM images of (a)-(d). (i) EDS mapping, (j) TEM image, (k) crystal fringes of (Ni, Fe)S_2@MoS_2 Mo:S-1:5.
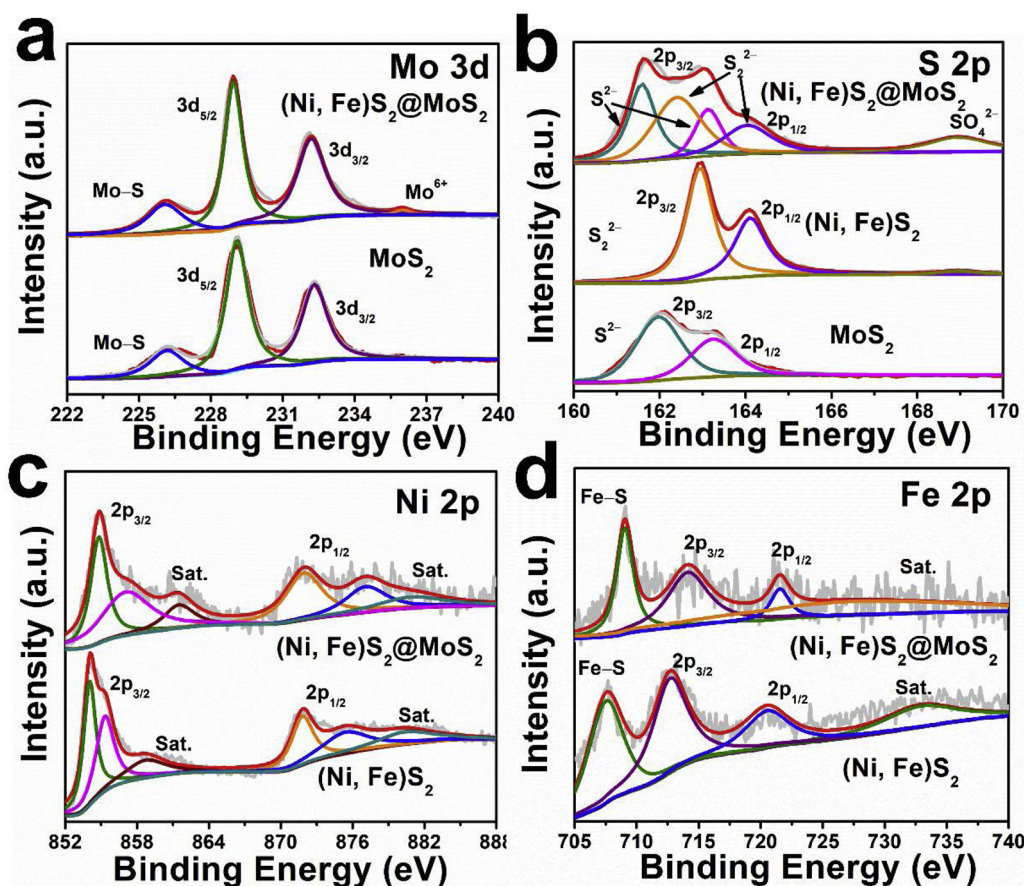
Fig. 3. XPS spectra of Mo 3d of (Ni, Fe)S$_2$@MoS$_2$ and MoS$_2$. (b) S 2p of (Ni, Fe)S$_2$@MoS$_2$, (Ni, Fe)S$_2$ and MoS$_2$. (c) Ni 2p and (d) Fe 2p of (Ni, Fe)S$_2$@MoS$_2$ and (Ni, Fe)S$_2$.

Mo 3d XPS spectra for MoS$_2$ and (Ni, Fe)S$_2$@MoS$_2$. The pure MoS$_2$ exhibits three peaks at 232.33, 229.13 and 226.23 eV, corresponding to Mo 3d$_{3/2}$, Mo 3d$_{5/2}$ and Mo-S, respectively [29,30]. After the formation of (Ni, Fe)S$_2$@MoS$_2$ core-shell nanostructure, all three peaks slightly shift to lower energy (232.31, 228.81 and 226.21 eV, respectively), representing the electron transfer from (Ni, Fe)S$_2$ to MoS$_2$. In addition, the peak at 236.47 eV is pertained to Mo^{6+}, which is possibly resulting from the surface oxidation [31]. As for the S 2p spectra, the (Ni, Fe)S$_2$@MoS$_2$ displays a superimposition of S^{2-} (161.61 and 163.11 eV) and S$_2^{2-}$ (162.41 and 164.01 eV), corresponding to MoS$_2$ and (Ni, Fe)S$_2$ respectively [32–34]. Both the S^{2-} and S$_2^{2-}$ shows negative shifts about 0.5 and 0.1 eV contrast to those of pure samples, indicating the strong interaction between (Ni, Fe)S$_2$ and MoS$_2$. It is worth mentioning that the various formations of S atoms could be apical S^{2-} and/or bridging S$_2^{2-}$, which could be explained to the active sites which is advantageous to HER process [35,36]. Besides, Ni 2p spectrum of (Ni, Fe)S$_2$@MoS$_2$ displays two pairs of peak: the peaks located at Ni 2p$_{1/2}$ (873.11 eV) and 2p$_{3/2}$ (855.01 eV) are corresponding to Ni^{2+}; and the peaks of Ni 2p$_{1/2}$ (878.61 eV) and 2p$_{3/2}$ (857.51 eV) are corresponding to Ni^{3+} (Fig. 3c). Both the binding energies of Ni^{2+} or Ni^{3+} show positive shifts in compared to those of (Ni, Fe)S$_2$ simple. Moreover, the peaks of Fe 2p$_{1/2}$ (721.01 eV) and Fe 2p$_{3/2}$ (713.51 eV) of (Ni, Fe)S$_2$@MoS$_2$ heterostructures also display positive shifts of 0.52 and 0.72 eV in compared to those of (Ni, Fe)S$_2$ sample (Fig. 3d), further confirm the electron transfer from (Ni, Fe)S$_2$ to MoS$_2$. As a result, the XPS spectra of as-prepared (Ni, Fe)S$_2$@MoS$_2$ reflect a strong interfacial interaction between (Ni, Fe)S$_2$ and MoS$_2$, which could be favorable to the overall water-splitting process.

3.2. Hydrogen evolution reaction (HER)

The HER performance of (Ni, Fe)S$_2$@MoS$_2$ was primarily tested in 1 M KOH for the purpose of recording the electrocatalytic activity for water splitting. The linear sweep voltammetry (LSV) curves of (Ni, Fe)S$_2$@MoS$_2$, (Ni, Fe)S$_2$, MoS$_2$ and Pt/C are displayed in Fig. 4a with IR modification. The (Ni, Fe)S$_2$@MoS$_2$ heterostructures need an clearly lower overpotential of 130 mV to reach 10 mA cm^{-2}, while (Ni, Fe)S$_2$ and MoS$_2$ demand overpotentials of 231 mV and 285 mV respectively (Fig. 4b). Even though the Pt/C electrode exhibits the highest activity at low current densities, the HER performance of (Ni, Fe)S$_2$@MoS$_2$ gets better than Pt/C to when delivering a high current densities (100 mA cm^{-2}) (Fig. 4b). We further investigate the HER performance in acidic media, which also illustrates the best HER activity of (Ni, Fe)S$_2$@MoS$_2$ (Fig. S7a). Moreover, the Tafel slop of (Ni, Fe)S$_2$@MoS$_2$ (101.22 mV dec^{-1}) is clear lower than those of (Ni, Fe)S$_2$ (144.19 mV dec^{-1}) and MoS$_2$ (183.80 mV dec^{-1}) (Fig. 4c), which indicates a more rapid HER catalytic rate and belongs to Volmer-Heyrovsky step. [37] To study the influence of interface engineering upon water-splitting process, HER performance of (Ni, Fe)S$_2$@MoS$_2$ heterostructures with different Mo contents are further investigated. As shown in Fig. 4d, the HER activity increases along with the extension of Mo:S from 0.25:5 to 1:5, but decreases after continually increasing to 3:5. The similar regular pattern also shows in acidic conditions (Fig. S7b), giving rise to the best HER performance for the sample of Mo:S-1:5. This suggests that an appropriate Mo content improves the electrocatalytic performance while an excessive one could impede HER process. Moreover, the as-obtained (Ni, Fe)S$_2$@MoS$_2$ heterostructures (Mo:S-1:5) require an overpotential of 130 mV to reach a current density of 10 mA cm^{-2}, which is 197, 145 and 22 mV smaller than that of (Ni, Fe)S$_2$@MoS$_2$ (Mo:S-0.25:5), (Ni, Fe)
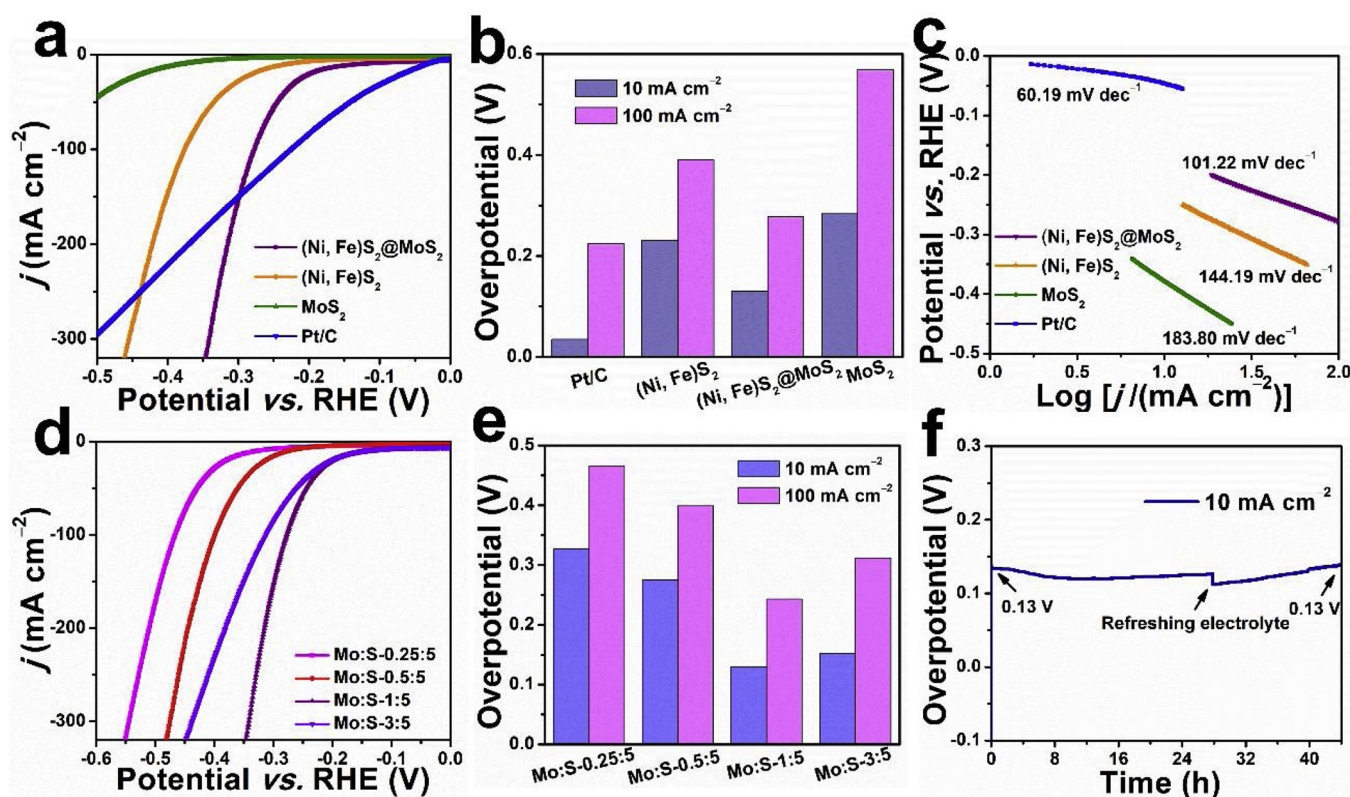
Fig. 4. (a) LSV curves, (b) Overpotentials at current densities of 10 mA cm^{-2} and 100 mA cm^{-2}, and (c) Tafel slops of (Ni, Fe)S$_2$@MoS$_2$, (Ni, Fe)S$_2$, MoS$_2$ and Pt/C. (d) LSV curves and (e) Overpotential at 10 mA cm^{-2} and 100 mA cm^{-2} of (Ni, Fe)S$_2$@MoS$_2$ (Mo:S-0.25:5, 0.5:5, 1:5 and 3:5). (f) Electrochemical stability test at 10 mA cm^{-2} of (Ni, Fe)S$_2$@MoS$_2$.

S$_2$@MoS$_2$ (Mo:S-0.5:5) and (Ni, Fe)S$_2$@MoS$_2$ (Mo:S-3:5), respectively (Fig. 4d). Similarly, the overpotenial of (Ni, Fe)S$_2$@MoS$_2$ (Mo:S-1:5) is also obviously lower than the other three samples at a high current density of 100 mA cm^{-2}. The long-term stability shows that it is maintains a well constant voltage of 0.13 V for 44 h at 10 mA cm^{-2} (Fig. 4f). Furthermore, (Ni, Fe)S$_2$@MoS$_2$ heterostructures that was tested under HER stability are nearly changeless (Fig. S8). Consequently, these results probe an excellent durability of the (Ni, Fe)S$_2$@MoS$_2$ catalyst during HER process under the alkaline environments.

3.3. Oxygen evolution reaction (OER)

The OER performance of (Ni, Fe)S$_2$@MoS$_2$ was tested in the same configuration compared with HER. As observed in Fig. 5a and b, the (Ni, Fe)S$_2$@MoS$_2$ core-shell electrode requires overpotential of 270 and 330 mV to achieve the current density of 10 and 100 mA cm^{-2} respectively, much lower than that of (Ni, Fe)S$_2$, MoS$_2$ and IrO$_2$. It should be noted that the overpotential was calculated based on the negative scanning polarization curve due to the interference of Ni^{3+}/Ni^{2+} redox peaks in the positive scanning (Fig. S9). The Tafel slop of (Ni, Fe)S$_2$@MoS$_2$ is 43.21 mV dec^{-1}, clearly smaller than that of (Ni, Fe)S$_2$ (107.58 mV dec^{-1}), MoS$_2$ (195.32 mV dec^{-1}) and IrO$_2$ (165.95 mV dec^{-1}) (Fig. 5c), suggesting enhanced OER kinetics for (Ni, Fe)S$_2$@MoS$_2$. In addition, the OER performance increases along with the extension of the ratio of Mo:S from 0.25:5 to 1:5, but decreases after continually increasing the ratio to 3:5 (Fig. S10). The stability test of (Ni, Fe)S$_2$@MoS$_2$ was carried out at 10 mA cm^{-2}, while it demonstrated a high OER overpotential in 1 M KOH and short-term stability (Fig. 5d). It should ascribe to the surface partial oxidation of (Ni, Fe)S$_2$ to NiFeO$_x$ during the OER process in the alkaline environment (Fig. 5e), which makes it necessary to stabilizing the sulfides to avoid the oxidation. To overcome this issue, we regulate the interface between the

electrolyte and electrode *via* adding the Na$_2$S into the electrolyte, which shows a remarkably improved stability performance with a nearly unchanged potential after a longer stability test of 44 h (just increased from 1.52 V to 1.55 V). It is worth mention that the adding of Na$_2$S to the electrolyte makes negligible interference to the OER and HER performances of (Ni, Fe)S$_2$@MoS$_2$ heterostructures (Fig. S11). Moreover, Faraday efficiency test was studied to determine whether the S ion was oxidized during OER process of (Ni, Fe)S$_2$@MoS$_2$. The yield of O$_2$ production is tested by using the water displacement approach in an air-tight reactor. As shown in Fig. S12, the calculated Faradaic efficiency can reach about 100% in the environment with Na$_2$S, demonstrating the introduced S ions in the electrolyte will not be oxidized under the water-splitting process. In addition, the morphology of the post-OER sample in electrolyte containing ionic S is nearly changeless (Fig. S13b, d), contrast to morphology destruction without ionic S (Fig. S13a, c). We propose that S atoms in the electrolyte provide a pathway to contact with the electrode instead of partial OH$^-$, to some extent, which avoid the S leaching from the surface of electrode as well as less oxidized interfacial areas during OER process.

3.4. Overall water splitting

As demonstrated above, the well-defined (Ni, Fe)S$_2$@MoS$_2$ heterostructures show both largely improved HER and OER activities. For the purpose of demonstrating their accessible applications of (Ni, Fe)S$_2$@MoS$_2$, a two-electrode electrolytic setup was constructed utilizing (Ni, Fe)S$_2$@MoS$_2$ as working electrode at the anode and cathode. The electrolyzer needs a potential of 1.56 V at 10 mA cm^{-2}, which is lower than (Ni, Fe)S$_2$||(Ni, Fe)S$_2$ (1.75 V), MoS$_2$||MoS$_2$ (1.93 V) and Pt/C||IrO$_2$ (1.76 V). Additionally, as shown in the insert of Fig. 5f, many bubbles pop up at both cathode and anode. Like the process of OER, when regulating the composition of electrolyte by adding Na$_2$S, the
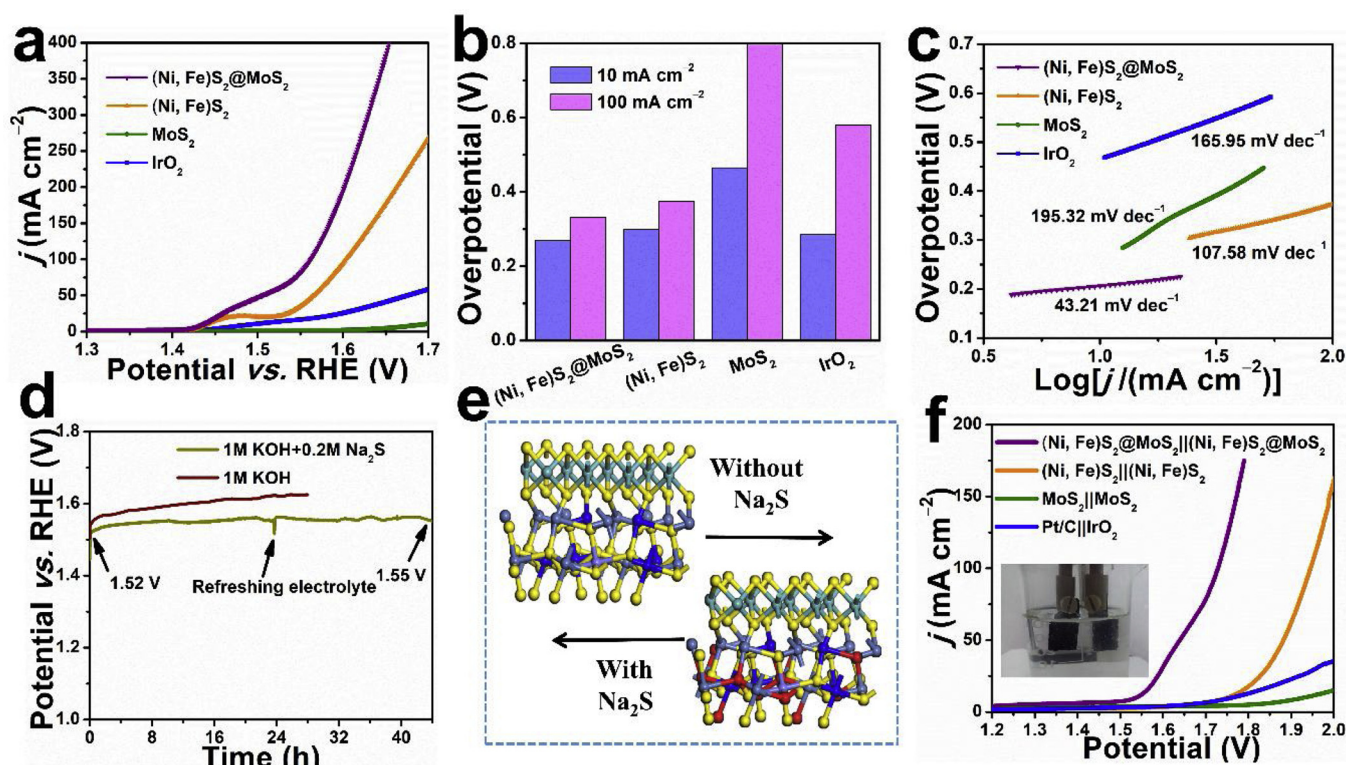
Fig. 5. (a) LSV curves, (b) overpotentials at the current densities of 10 mA cm^{-2} and 100 mA cm^{-2}, and (c) Tafel slops for (Ni, Fe)S$_2$@MoS$_2$, (Ni, Fe)S$_2$, MoS$_2$ and Pt/C. (d) Stability test of different electrolytes for (Ni, Fe)S$_2$@MoS$_2$. (e) The proposed scheme of the structural transformation of (Ni, Fe)S$_2$@MoS$_2$ in different electrolytes during OER process (Yellow: S, Red: O, Dark blue: Fe, Light blue: Ni and Dark cyan: Mo). (f) LSV curves of two-electrode cell assembled by different materials (inset: the optical image of two-electrode setup) (For interpretation of the references to colour in this figure legend, the reader is referred to the web version of this article).

durability of water-splitting is more stable than electrolyte without Na$_2$S, which means the interface engineering of electrolyte and electrode plays an important role in stability of sulfides electrocatalysts (Fig. S14).

3.5. Discussion

To understand the electron transportation capability, electrochemical impedance spectroscopy (EIS) spectra were carried out and relevant Nyquist plots were recorded in Fig. 6a. The curves of (Ni, Fe)S$_2$@MoS$_2$, (Ni, Fe)S$_2$ and MoS$_2$ include a semicircle suggesting charge-transfer resistance (R_{ct}) in high frequency region, and the slope of straight line in the low frequency region implying ion diffusion resistance. The (Ni, Fe)S$_2$@MoS$_2$ heterostructures show the smallest R_{ct}, which indicates their faster electron transport kinetic and intrinsic excellent electron conductivity. The conclusions are highly consistent with their LSV behaviors (Figs. 4a and 5 a). Additionally, the electrochemical double layer capacitance (C_{dl}) was conducted to evaluate the electrochemical surface area (ECSA) (Fig. S15). (Ni, Fe)S$_2$@MoS$_2$ heterostructures show the largest ECSA (0.67 m F cm^{-2}), which gives 1.8 and 2.7 times higher C_{dl} than that of (Ni, Fe)S$_2$ (0.37 m F cm^{-2}) and MoS$_2$ (0.25 m F cm^{-2}) (Fig. 6b). Thus, these results show that interface engineering between (Ni, Fe)S$_2$ and MoS$_2$ account for an enhanced electrochemical surface area. Furthermore, to investigate the influence of interface engineering upon electron transportation ability, the Nyquist plots of different Mo contents are shown in Fig. S16a. The (Ni, Fe)S$_2$@MoS$_2$ heterostructures (Mo:S-1:5) have the smallest semicircle compared with the other three samples, which means it has the fastest electron transportation ability. Likewise, the increase in ECSA from (Ni, Fe)S$_2$@MoS$_2$ (Mo:S-0.25:5) to (Ni, Fe)S$_2$@MoS$_2$ (Mo:S-1:5) can be attributed to the enhanced interfacial areas. To be contrast, the resistance increases and the C_{dl} decreases along with further elongation the ratio

of Mo:S (Fig. S16b), which is consistent with HER and OER performance (Figs. 4d and S10). Thus, the interface engineering facilitates a rapid electron transfer and active sites exposure.

The electronic interaction between (Ni, Fe)S$_2$ and MoS$_2$ could also weaken S-H$_{ads}$ formed on the interface, which regulates H chemisorption to facilitate the Volmer-Heyrovsky process. *In-situ* Raman spectra were applied to investigate the bonding formation of S-H$_{ads}$ intermediate at the interface between (Ni, Fe)S$_2$ and MoS$_2$ (Fig. 6c). No peak is detected when there is no potential applied to the electrode at the range from 2000 cm^{-1} to 2700 cm^{-1}. Similarly, when the potential recorded −1.0 V *vs.* Ag/AgCl, which is slightly positive than HER theoretical hydrogen evolution potential, there was no effective peaks could be found. However, when we changed the potential to −1.5 V, there were some bubbles popping up at the surface of electrode and Raman spectra could be detected some peaks due to bubbles covering the surface, at this time we assume S-H$_{ads}$ has formed [38]. Subsequently, when increasing the potential back to −1.2 V, it is clearly that a peak around 2574 cm^{-1} is found for (Ni, Fe)S$_2$@MoS$_2$, which could be resulted from the accumulated S-H$_{ads}$ of high potential. Finally, we continually increased the potential to −1.0 V, no obvious peak means that the accumulated S-H$_{ads}$ has been depleted. It is worth claiming that the negative shift of S-H$_{ads}$ of (Ni, Fe)S$_2$@MoS$_2$ (2574 cm^{-1}) compared with that of (Ni, Fe)S$_2$ (2577 cm^{-1}) and MoS$_2$ (2646 cm^{-1}), implying that the S-H$_{ads}$ bonds on (Ni, Fe)S$_2$@MoS$_2$ are weaker than those on (Ni, Fe)S$_2$ and MoS$_2$ (Fig. 6d) [39,40]. Thus, the *in-situ* Raman spectra verify that the (Ni, Fe)S$_2$@MoS$_2$ heterostructures are favorable to H adsorption and the formation of S-H$_{ads}$ for efficient overall water splitting.

4. Conclusion

In summary, well-defined (Ni, Fe)S$_2$@MoS$_2$ heterostructures have been successfully synthesized by using NiFe-LDH as the precursor. As a
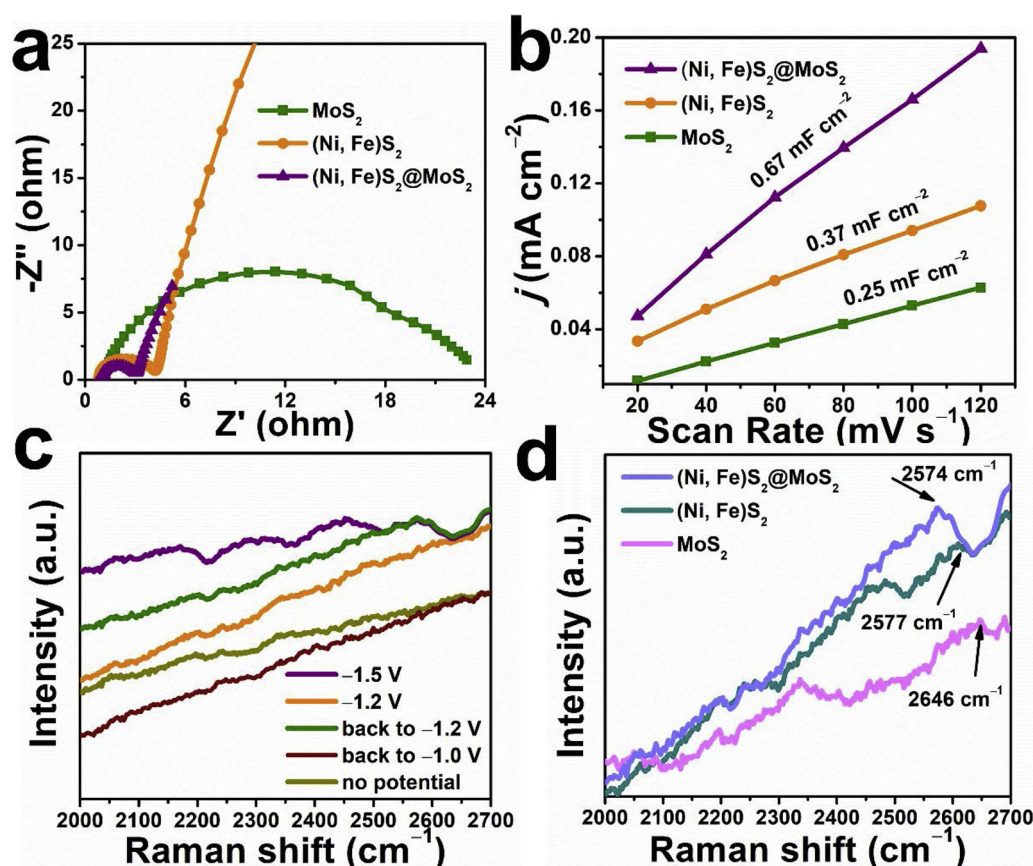
Fig. 6. (a) Nyquist plots obtained by electrochemical impedence spectroscopy (EIS), (b) double layer capacitance (C_{dl}) of MoS_2, (Ni, Fe)S_2 and (Ni, Fe)$S_2@MoS_2$, (c) *In-situ* Raman spectra at different potentials at range of 2000–2700 cm^{-1}, (d) *In-situ* Raman spectra at 2000–2700 cm^{-1} for (Ni, Fe)$S_2@MoS_2$, (Ni, Fe)S_2 and MoS_2.

result, the (Ni, Fe)$S_2@MoS_2$ electrode with Mo:S-1:5 displays a remarkable performance and durability for both HER and OER under basic environments. Furthermore, as-obtained (Ni, Fe)$S_2@MoS_2$ heterostructures with rich active sites provide favorable chemisorption of hydrogen, resulting easy formation of S-H$_{ads}$ in alkaline environments. In addition, the interface regulation of (Ni, Fe)$S_2@MoS_2$/electrolyte through changing the composition of electrolyte significantly promotes the electrochemical stability of sulfides electrocatalyst. It is expected that the approach of interface engineering could be extended to design low-cost, high-efficiency and long-term stability bifunctional electrocatalysts with potential applications.

Conflict of interest

The authors declare no conflict of interest.

Acknowledgements

Appendix A. Supplementary data

Supplementary material related to this article can be found, in the online version, at doi:https://doi.org/10.1016/j.apcatb.2019.01.094.

References

[1] J.A. Turner, Science 305 (2004) 972–974.
[2] A. Kudo, Y. Miseki, Chem. Soc. Rev. 38 (2009) 253–278.
[3] H. Yin, S. Zhao, K. Zhao, A. Muqsit, H. Tang, L. Chang, H. Zhao, Y. Gao, Z. Tang, Nat. Commun. 6 (2015) 6430.
[4] M. Walter, E. Warren, J. McKone, S. Boettcher, Q. Mi, E. Santori, N. Lewis, Chem. Rev. 110 (2010) 6446–6473.
[5] L. Zhao, J. Jia, Z. Yang, J. Yu, A. Wang, Y. Sang, W. Zhou, H. Liu, Appl. Catal. B: Environ. 210 (2017) 290–296.
[6] G. Li, J. Yu, J. Jia, L. Yang, L. Zhao, W. Zhou, H. Liu, Adv. Funct. Mater. 28 (2018) 1801332.
[7] O. Diaz-Morales, S. Raaijman, R. Kortlever, P. Kooyman, T. Wezendonk, J. Gascon, W. Fu, M. Koper, Nat. Commun. 7 (2016) 12363.
[8] I. Ledezma-Yanez, W. Wallace, P. Sebastián-Pascual, V. Climent, J. Feliu, M. Koper, Nat. Energy 2 (2017) 17031.
[9] J. Tian, Q. Liu, A.M. Asiri, X. Sun, J. Am. Chem. Soc. 136 (2014) 7587–7590.
[10] A. Sivanantham, S. Shanmugam, Appl. Catal. B: Environ. 203 (2017) 485–493.
[11] G. Zhang, P. Wang, W. Lu, C. Wang, Y. Li, C. Ding, J. Gu, X. Zheng, F. Cao, ACS Appl. Mater. Interfaces 9 (2017) 28566–28576.
[12] C. Tang, N. Cheng, Z. Pu, W. Xing, X. Sun, Angew. Chem. Int. Ed. 54 (2015) 9351–9355.
[13] G. Zhang, Y. Feng, W. Lu, D. He, C. Wang, Y. Li, X. Wang, F. Cao, ACS Catal. 8 (2018) 5431–5441.
[14] L. Yang, W. Zhou, J. Lu, D. Hou, Y. Ke, G. Li, Z. Tang, X. Kang, S. Chen, Nano Energy 22 (2016) 490–498.
[15] Q. Lu, Y. Yu, Q. Ma, B. Chen, H. Zhang, Adv. Mater. 28 (2016) 1917–1933.
[16] D. Voiry, J. Yang, M. Chhowalla, Adv. Mater. 28 (2016) 6197–6206.
[17] M. Lukowski, A. Daniel, F. Meng, A. Forticaux, L. Li, S. Jin, J. Am. Chem. Soc. 135 (2013) 10274–10277.
[18] D. Voiry, M. Salehi, R. Silva, T. Fujita, M. Chen, T. Asefa, V. Shenoy, G. Eda, M. Chhowalla, Nano Lett. 13 (2013) 6222–6227.
[19] H. Wang, Q. Zhang, H. Yao, Z. Liang, H. Lee, P. Hsu, G. Zheng, Y. Cui, Nano Lett. 14 (2014) 7138–7144.
[20] G. Li, D. Zhang, Q. Qiao, Y. Yu, D. Peterson, A. Zafar, R. Kumar, S. Curtarolo, F. Hunte, S. Shannon, Y. Zhu, W. Yang, L. Cao, J. Am. Chem. Soc. 138 (2016) 16632–16638.
[21] H. Li, C. Tsai, A. Koh, L. Cai, A. Contryman, A. Fragapane, J. Zhao, H. Han, H. Manoharan, F. Abild-Pedersen, J. Nørskov, X. Zheng, Nat. Mater. 15 (2016) 364.
[22] X. Geng, W. Sun, W. Wu, B. Chen, A. Al-Hilo, M. Benamara, H. Zhu, F. Watanabe, J. Cui, T. Chen, Nat. Commun. 7 (2016) 10672.
[23] M. Gong, Y. Li, H. Wang, Y. Liang, J. Wu, J. Zhou, J. Wang, T. Regier, F. Wei, H. Dai, J. Am. Chem. Soc. 135 (2013) 8452–8455.
[24] Q. Wang, L. Shang, R. Shi, X. Zhang, G.I.N. Waterhouse, L. Wu, C. Tung, T. Zhang,

Nano Energy 40 (2017) 382–389.

[25] X. Jia, Y. Zhao, G. Chen, L. Shang, R. Shi, X. Kang, G.I.N. Waterhouse, L. Wu, C. Tung, T. Zhang, Adv. Energy Mater. 6 (2016) 1502585.

[26] Z. Lu, W. Xu, W. Zhu, Q. Yang, X. Lei, J. Liu, Y. Li, X. Sun, X. Duan, Chem. Commun. 50 (2014) 6479–6482.

[27] L. Zhou, M. Shao, C. Zhang, J. Zhao, S. He, D. Rao, M. Wei, D. Evans, X. Duan, Adv. Mater. 29 (2017) 1604080.

[28] B. Li, S. Zhang, C. Tang, X. Cui, Q. Zhang, Small 13 (2017) 1700610.

[29] H. Zhu, J. Zhang, R. Zhang, M. Du, Q. Wang, G. Gao, J. Wu, G. Wu, M. Zhang, B. Liu, J. Yao, X. Zhang, Adv. Mater. 27 (2015) 4752–4759.

[30] G. Li, D. Zhang, Q. Qiao, Y. Yu, D. Peterson, A. Zafar, R. Kumar, S. Curtarolo, F. Hunte, S. Shannon, Y. Zhu, W. Yang, L. Cao, J. Am. Chem. Soc. 138 (2016) 16632–16638.

[31] Y. Guo, J. Tang, H. Qian, Z. Wang, Y. Yamauchi, Chem. Mater. 29 (2017) 5566–5573.

[32] T. Wang, J. Zhuo, K. Du, B. Chen, Z. Zhu, Y. Shao, M. Li, Adv. Mater. 26 (2014) 3761–3766.

[33] L. Ting, Y. Deng, L. Ma, Y. Zhang, A. Peterson, B. Yeo, ACS Catal. 6 (2016) 861–867.

[34] L. Sun, T. Wang, L. Zhang, Y. Sun, K. Xu, Z. Dai, F. Ma, J. Power Sources 377 (2018) 142–150.

[35] Z. Huang, W. Luo, L. Ma, M. Yu, X. Ren, M. He, S. Polen, K. Click, B. Garrett, J. Lu, K. Amine, C. Hadad, W. Chen, A. Asthagiri, Y. Wu, Angew. Chem. Int. Ed. 54 (2015) 15181–15185.

[36] J. Hu, B. Huang, C. Zhang, Z. Wang, Y. An, D. Zhou, H. Lin, M. Leung, S. Yang, Energy Environ. Sci. 10 (2017) 593–603.

[37] M. Chialvo, A. Chialvo, J. Electroanal. Chem. 372 (1994) 209–223.

[38] J. Feng, J. Wu, Y. Tong, G. Li, J. Am. Chem. Soc. 140 (2018) 610–617.

[39] Y. Deng, L. Ting, P. Neo, Y. Zhang, A. Peterson, B. Yeo, ACS Catal. 6 (2016) 7790–7798.

[40] Y. Deng, B. Yeo, ACS Catal. 7 (2017) 7873–7889.